

---

## Analysis of Dual-Frequency Ocean Backscatter Measurements at Ku- and Ka-Bands Using Near-Nadir Incidence GPM Radar Data

Nouguier Frédéric<sup>1,2,\*</sup>, Mouche Alexis<sup>3</sup>, Rasclé Nicolas<sup>3</sup>, Chapron Bertrand<sup>3</sup>, Vandemark Douglas<sup>4</sup>

<sup>1</sup> Mediterranean Inst Oceanog, F-13288 Marseille, France.

<sup>2</sup> Univ Toulon & Var, CNRS INSU, IRD, F-83957 La Garde, France.

<sup>3</sup> IFREMER, Lab Oceanog Spatiale, F-29280 Plouzane, France.

<sup>4</sup> Univ New Hampshire, Inst Study Earth Oceans & Space, Durham, NH 03824 USA.

\* Corresponding author : Frédéric Nouguier, email address : [frederic.nouguier@gmail.com](mailto:frederic.nouguier@gmail.com)

---

### Abstract :

Global colocalized ocean surface measurements using the Global Precipitation Measurement near-nadir dual-frequency Ku- and Ka-band microwave measurements are analyzed and compared. Focusing on the Ka and Ku cross-sections fall-off with incidence angles, the contemporaneous measurements enable to more precisely document differing ocean scattering characteristics for both microwave frequencies. Sensitivity with wind speed and significant wave height is further reported using global comparisons with numerical estimates. As demonstrated, the bifrequency capability can provide direct means to efficiently separate short-scale wave contributions, between mean squared slope and curvature characteristics, and to further gain valuable insights concerning near-nadir instruments onboard future ocean satellite missions including the China-France Oceanography Satellite and the Surface Water Ocean Topography Mission.

**Keywords :** Microwave, radar cross section, scattering, spaceborne radar

### 1 Introduction

---

This note attempts to isolate and interpret subtle but measurable wind-dependent differences between near-nadir ocean radar backscatter data observed at Ku- and Ka-band. The interpretation involves inference of ocean surface wave slope and curvature statistics assuming quasi-specular radar reflection from the sea. This new global view of sea surface microwave scattering at short cm to mm

frequencies is provided by the Dual-frequency Precipitation Radar (DPR) onboard the Global Precipitation Measurement (GPM) mission satellite platform. With exactly matching surface antenna footprints at and around nadir incidence angles, the Ku- and Ka-band PR normalized radar cross section ( $\sigma^0$ ) measurements enable systematic and co-localized analysis of differing ocean scattering characteristics. As shown in this letter, bi-frequency data analysis appears to provide a means to separate surface slope and curvature effects. This can lead to a refined estimation of the fine scale sea surface roughness at the cm-scale that is in turn related to physical air-sea processes such as the local wind stress and the rate of gas exchange across the sea surface.

The present study builds on previous satellite observations where the new DPR data now combines dual frequency and incidence angle diversity that were before separated. For example, dual-frequency altimeter (nadir only)  $\sigma^0$  observations and analyses used global sampling obtained using TOPEX ([1, 2]), at both C- and Ku-band along with significant wave height estimates, to suggest an approach that better isolates short-scale wind wave information and can lead to improved wind speed estimates (e.g., [3, 4, 5]). As understood, if very short scale roughness elements were not present, wind-dependent returns at both frequencies would be identical. However, clear wind dependency is systematically observed for the ratio  $\sigma^0_C/\sigma^0_{Ku}$ . Analyses of this C-Ku combination ([1, 2]) points out that the critical surface wave length scales of interest must lie in the short gravity-capillary wave range.

Additional near-nadir data has been provided by the large TRMM KuPR dataset. Using TRMM, it is possible to use spaceborne rain radar data to obtain Ku-band microwave ocean surface  $\sigma^0$  measurements across a small but important range of near-nadir incidence angles ([6]). The added angular information provides for a more complete analysis under the quasi-specular scattering framework. Moreover, [7] colocalized satellite altimeter-derived significant wave height with TRMM data to document the impacts of both wind speed (short wave) and longer-scale gravity waves on  $\sigma^0$  and its variation with incidence angle. Chu et al. [8, 9] then extended this analysis to study asymmetry and anisotropy of the Ku-band near-nadir backscatter signals.

Now, the DPR onboard GPM provides systematic co-localized Ka- and Ku-band measurements leading to large and statistically meaningful data sets, and data covering the same range of incidence angles ( $0^\circ - 9^\circ$ ) provided by TRMM. To exploit both bi-frequency and incidence angle aspects of the GPM DPR, we propose to use a method similar to [10, 11] that relies foremost on the analysis of  $\sigma^0$  incidence fall-off to derive sea surface parameters. This relaxes the need to have precisely inter-calibrated Ku- and Ka-band measurements, and for instance the known differing SST impact on Ka- and Ku-band Fresnel coefficients (e.g. [12]).

Section 2 presents an overview of the Ku- and Ka-band  $\sigma^0$  measurements and global comparisons with numerical wind and wave parameter estimates. Section 3 uses an extended Physical Optics (PO) scattering approach to develop an interpretation of GPM  $\sigma^0$  fall-off sensitivity at both frequencies that includes relating these high frequency microwave observations to the well known Cox &

Munk measurements [13]. We then demonstrate that a bi-frequency analysis can be used to separate long and short scale roughness element impacts on GPM  $\sigma^0$ , with the new result being the capability to better infer total sea surface mean squared slope and the influence of small-scale curvature.

## 2 GPM, an opportunity for ocean remote sensing

### 2.1 GPM Ku and Ka DPR

Launched on 2014, February 27th, the GPM mission provides new and unexplored data over the ocean. While the GPM mission is primarily designed to provide new information on rain and snow precipitation estimates, the ocean remote sensing community can also explore this new global source of information on ocean backscatter.

The GPM platform carries the first space-borne Ku/Ka-band Dual-frequency Precipitation Radar (DPR) and a multi-channel Microwave Imager (GMI). In particular, the KaPR operates at 35.5 GHz with a nadir oriented antenna. The  $0.7^\circ$  beamwidth antenna sweeps a 120 km swath providing a  $5 \text{ km} \times 5 \text{ km}$  surface footprint. The KuPR, co-aligned with the KaPR, operates at 13.6 GHz and provides a wider 245 km swath but with the same  $5 \text{ km} \times 5 \text{ km}$  resolution. As designed, KuPR and KaPR have 25 matched beams to provide perfectly co-localized Ku/Ka measurements for incidence angles between  $-9$  and  $9^\circ$ .

For this study, selected data correspond to the Nominal Swath (NS) of the KuPR and the co-localized Matched Swath (MS) of the KaPR. Acquisitions over land, ice, and raining regions as well as those with flagged as poor quality were removed, leading to 165157 points for the Ku-band set and 85729 points for the Ka-band set.

### 2.2 Ocean wave model colocation and data analysis

For all selected points, outputs of the *Wave Watch III* (WW3) ocean surface wave model were coregistered with GPM to provide surface wind speed and significant wave height estimates. The WW3 model output was provided with a 0.5 degree / 1h spatio-temporal resolution.

Figure 1 shows the nearest-to-nadir incidence ( $\theta = 0.7^\circ$ ) Ka-band  $\sigma^0$  versus significant wave height (SWH) for different wind speeds. As expected, Ku- (not shown here) and Ka-band  $\sigma^0$  measurements are sensitive to both wind speed and the sea state's degree of development, i.e. SWH. The latter sensitivity of  $\sigma^0$  to SWH decreases with increasing wind speed, and also for higher incidence angles (up to 9 degrees, not shown), consistent with previous studies ([7], [8, 9]). However, at a given SWH, the  $\sigma^0$  changes with wind speed are found to be slightly higher at Ka- than for Ku-band. This is in line with results recently reported by [14] using SARAL-Altika and ENVISAT-RA altimeter measurements.

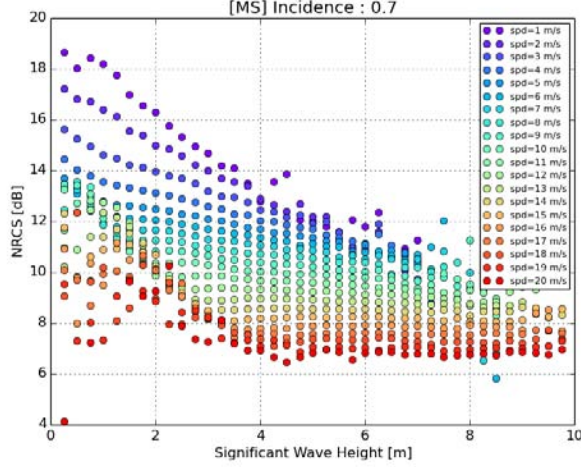


Figure 1: KaPR  $\sigma^0$  versus significant wave height at  $\theta = 0.7^\circ$

### 3 Physical interpretation

#### 3.1 An adapted scattering model

The Geometrical Optics (GO) approximation for electromagnetic (EM) scattering from rough sea surfaces is still widely used to interpret nadir and near-nadir microwave radar measurements ([15]). A GO model solely relates the radar cross section to the sea surface slope probability distribution function and should thus be insensitive to the EM radar wavelength (except for the the impact of seawater permittivity). For mm-wave (Ka-band) sensors and ocean surfaces, where the known roughness elements are longer than 5 mm or so, this optical assumption should be quite valid, effectively approaching the response of VIS sensors. Hereafter, we briefly recall the GO formulation.

Denoting  $\mathbf{K}_0$  and  $\mathbf{K}$  as the incident and scattered EM wave vectors, and then their respective horizontal  $\mathbf{k}_0$ ,  $\mathbf{k}$  and vertical  $-q_0$ ,  $q$  components, one has:

$$\mathbf{K}_0 = \mathbf{k}_0 - q_0 \hat{\mathbf{z}}, \quad \mathbf{K} = \mathbf{k} + q \hat{\mathbf{z}}, \quad (1)$$

with  $q, q_0 > 0$  and  $k_0^2 + q_0^2 = k^2 + q^2 = K_0^2$ , and one can define the Ewald vector  $\mathbf{Q} = \mathbf{K} - \mathbf{K}_0$  with horizontal  $\mathbf{Q}_H = \mathbf{k} - \mathbf{k}_0$  and vertical  $Q_z = q + q_0$  components. The GO approximation can then becomes

$$\sigma^0 = \frac{4\pi|\mathcal{K}|^2}{Q_z^4} P_{\eta'} \left( \frac{\mathbf{Q}_H}{Q_z} \right) \quad (2)$$

where  $P_{\eta'}$  is the bi-dimensional slope probability density function (PDF) of the surface and  $\mathcal{K}$  is the Kirchhoff kernel related to the Fresnel coefficient.  $\mathcal{K}$  depends on both the incidence angle and EM frequency. Under an isotropic

Gaussian assumption for the sea surface slope distribution, equation (2) simplifies to:

$$\sigma^0 = \frac{|R|^2}{\text{mss}_T} \sec^4(\theta) \exp\left(-\frac{\tan^2(\theta)}{\text{mss}_T}\right) \quad (3)$$

where  $\theta$  is the radar incidence angle,  $\text{mss}_T$  is the total mean square slope and  $|R|$  is the Fresnel coefficient at normal incidence.

This form (3) supports the popular and robust approach to use a Gaussian fit with  $\theta$  to analyze  $\sigma^0$  in the micro-wave regime. However, as generally reported, the shape of the logarithm of the near-nadir  $\sigma^0$  fall-off is indeed very close to the parabolic-gaussian approximation, but with a faster fall-off compared to optical measurements. The estimate parameter, called  $\text{mss}_{\text{shape}}$  hereafter, is always smaller than its optical counterpart :  $\text{mss}_T$ .

The commonly invoked physical interpretation of this discrepancy from the optical assumption is that the longer EM wavelength acts like a physical filtering/sampling of the surface roughness spectrum, in effect shorter elements remain unseen. An alternative explanation is given in [16] where they posit that non-Gaussianity in the sea surface slope distribution could produce similar deviation in  $\sigma^0$  fall-off with  $\theta$  ([11]).

For this study a first-order correction to the GO model for curvature impact is next imposed based on the Physical Optics formulation (i.e. GO4 model [17]). For the isotropic case and considering the correction to be small, a Gram-Charlier development can be used and written as:

$$\begin{aligned} \sigma^0 &= \frac{|R|^2 \sec^4(\theta)}{\text{mss}_T} \exp\left(-\frac{\tan^2(\theta)}{\text{mss}_T}\right) \times \\ &\left[1 + \frac{\alpha}{4} \left(\frac{\tan^4(\theta)}{\text{mss}_T^2} - 4\frac{\tan^2(\theta)}{\text{mss}_T} + 2\right)\right] \end{aligned} \quad (4)$$

where

$$\alpha = \frac{2\lambda_4}{3} + \frac{\text{msc}}{Q_z^2 \text{mss}_T^2} \quad \text{with} \quad Q_z = 2K_0 \cos(\theta) \quad (5)$$

with a correction that encompasses  $\lambda_4$ , a kurtosis (frequency-independent) coefficient that can be related to the  $c_{04}$  and  $c_{40}$  (eq. (12) in [15]). These are the fourth order statistical parameters introduced by [13] ( $\lambda_4 = c_4$ ). The right hand term holds a frequency-dependent correction related to  $\text{msc}$ , a parameter directly linked to the short-scale sea surface mean squared curvature. This correction term vanishes as the EM wavelength approaches sub-mm wavelengths. Note also that the isotropic assumption cancels out the skewness coefficient introduced by [13]. To interpret this GO4 modification, if one assumes the overall statistical and geometrical correction sufficiently small (e.g. for Ka-band measurements) and also considers only shallow small incidence angles, a direct identification of the  $\tan^2(\theta)$  factor in equation (4) leads to:

$$\text{mss}_{\text{shape}} \simeq \text{mss}_T \div (1 + \alpha) \quad (6)$$

Equations (6) and (5) explain why the shape parameter is always smaller than the total mean square slope. According to equation (5), this difference

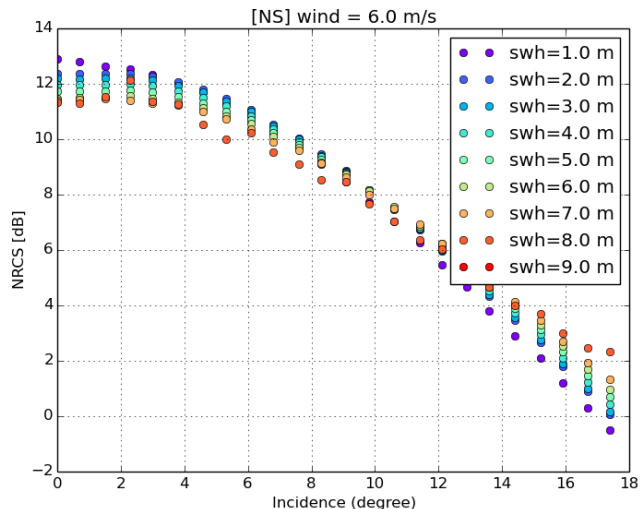


Figure 2: KuPR  $\sigma^0$  versus incidence at  $U_{10} = 6 \text{ m.s}^{-1}$

can be attributed to both the non-Gaussian nature of the surface (kurtosis  $\lambda_4$ ), independent of the EM wavelength, and a frequency-dependent correction due to both surface curvature and slope. Thus, as interpreted, the shape parameter does not necessarily correspond to a particular statistical parameter linked to a filtered surface, and/or a precise facet-size definition. For low surface curvature conditions and large EM frequency,  $\alpha$  reduces to solely a non-Gaussian surface correction. The pure tangent-plane approximation holds, and the GO model is recovered. But if the mean squared curvature correction term increases and/or  $Q_z$  decreases, then  $\alpha$  will increase and the PO model departs from GO. While weak, polarization sensitivity ([18]) is also expected. Accordingly, the key parameter controlling GO-departure is  $\alpha$ , and this parameter will be much larger for Ku- than for Ka-band measurements ( $Q_z$  effect). At Ku-band, the roughness correction is almost 10 times larger than at Ka-band. So the simplified Gram-Charlier development (4) does not necessarily hold. However, contemporaneous Ku- and Ka-band measurements from GPM may hold information to refine characterization of the wind-dependence in fine scale wavelets present on the surface.

### 3.2 Shape parameter

As illustrated in figure (2), the  $\sigma^0$  dependence with incidence angle closely follows the expected parabolic-shape assumption for both Ka and Ku bands and for a wide range of wind speeds ( $0 < U_{10} < 18 \text{ m.s}^{-1}$ ) and SWH ( $0 < \text{SWH} < 6.5 \text{ m}$ ). The form of equation (3) appears to agree well with the observed incidence fall-off of  $\sigma^0$  and so we can invert the shape parameter  $\text{mss}_{\text{shape}}$  using a linear

regression in the  $(\log(\cos^4(\theta)\sigma^0), \tan^2(\theta))$  domain (the  $mss_{shape}$  corresponds to the inverse of the slope coefficient). However, deviations from the Gaussian law are most noticeable for very low sea states and/or at the largest incidence angles. In these cases, the  $mss_{shape}$  parameter is the dominant term in the decrease of  $\sigma^0$  with angle and its estimate depends on the range of angles used in the regression. To avoid this artifact, the Student's t- Distribution is used on data over the full range of incidence angles ([16]). This distribution can account for deviations from parabolic behavior at off-nadir angles while maintaining parabolic dependence near nadir. The retrieval of the shape parameter from this regression is robust with respect to the range of incidence angles that are used.

Figure 3 displays the resulting  $mss_{shape}$  as a function of wind speed and sea state for the Ku- and Ka- bands. It clearly illustrates, for both bands, variability in the shape parameter with the SWH under low wind speed conditions. With increasing wind speed, shorter scale waves will start to exhibit larger slopes. Steep short-scale waves are more strongly coupled with the wind speed ([19]) and become the dominant contribution to the shape mean square slope. The result is a lower relative dependency of  $mss_{shape}$  on SWH variation under higher wind speed conditions.

The blue points in figure 3 represent the so-called total mean square slope estimates. They are provided as reference estimates based on the optically-based measurements reported by [13]. As discussed in [20], Cox and Munk could not directly measure the occurrence of the very infrequent steepest wave slopes with sufficient accuracy to include these important contributors to the total slope PDF. Thus a so-called *blanket* procedure, also including the non-gaussian contributions, was used to produce an ad hoc normalized PDF (see [16], for a more detailed discussion). This extra-contribution is wind independent and simply involves the application of a constant (enhancement) of  $\sim 1.23$ . This factor relates their (measured) optical shape parameter to the (expected) total mean squared slope parameter. The grey stars on figure 3 thus represent the "C&M  $mss_{shape}$ ", as derived from their data in the non-normalized distribution and as obtained in the optical domain.

As for the Cox & Munk experiment, GPM bi-frequency data does not cover sufficiently large incidence angles. Thus, even if one includes the PO correction term carrying the curvature effect, when one uses the smallest incidence angles (see equation (4)), the total mean square slope is difficult to recover using the regression of  $\sigma^0$  fall-off. Accordingly, this Ku- and Ka-band  $mss_{shape}$  is best compared to the  $mss_{shape}$  derived from optical measurements. This most direct comparison should first help to assess the non-Gaussian correction that should be common to all measurements. As obtained, this indeed helps to better reconcile optical and high-frequency microwave data analysis. Especially at low wind speeds, scales involved in the scattering process are mostly larger than the EM wavelengths. The  $\sigma^0$  fall-off is then similar for the two microwave bands as well as for the optical case. It results in very close  $mss_{shape}$  values for the three acquisitions. Note that Cox and Munk measurements do not exhibit SWH variability. This is because their data, acquired over a coastal area, were mainly

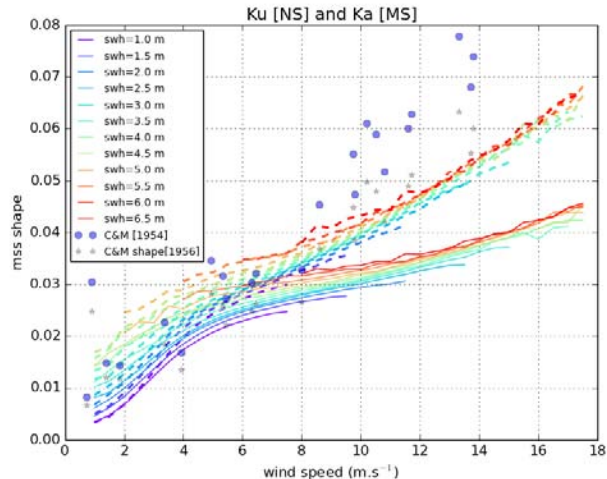


Figure 3: Mss shape versus wind speed for different SWH. Colored curves are derived from the regression of the Ku/Ka DPR incidence variations. Solid lines stand for the Ku-band and dashed lines for Ka-. Blue points are C&M 54 reference points. Grey stars are C&M points without kurtosis correction, i.e. their  $mss_{shape}$ .

obtained under low sea state conditions.

For wind speeds larger than  $7 \text{ m.s}^{-1}$ , the  $mss_{shape}$  for both Ku- and Ka-band are systematically observed to be smaller than for optical. However, as expected, the correction related to the finite scale of the EM wavelength and the growth of short-scale roughness elements leads to a lower  $mss_{shape}$  value for the Ku- (2.2 cm) than the Ka-band (8.4 mm) measurements.

This is further illustrated by considering the difference between  $mss_{shape}$  at the two frequencies:

$$\Delta mss_{shape} = mss_{shape-Ka} - mss_{shape-Ku} \quad (7)$$

As developed, this difference is expected to eliminate non-Gaussian impacts, and is directly related to deviation from the GO approximation due to short-scale curvature effects. Figure 4 illustrates this difference  $\Delta mss_{shape}$  (7) against wind speed for the different SWH classes. As observed, the strong SWH dependence is now severely attenuated. Indeed, the longer waves that dominate SWH and are often dissociated from the local wind field, are certainly equally resolved by the individual microwave instruments. However, this  $\Delta mss_{shape}$  measurement efficiently cancels this long wave contribution. The remaining signal is then frequency dependent small-scale roughness corrections. Mostly starting above a wind speed of 7 m/s, these corrections are then likely dominated by the growth in steep short surface roughness scales, possibly exhibiting high curvature near their crests [21], but also possibly due to enhanced generation of short-crested

surface roughness disturbances generated by breaking waves, including parasitic capillary waves [19].

Foremost, to retrieve the total  $mss$  from GPM measurements remains challenging. The mathematical approximation (4) is certainly justified for Ka-band, but likely limited for Ku-band. The GPM incidence excursion of the Ka-band (9 degrees) is also too small to help derive precise curvature and slope variance parameters. More quantitatively, it is the difference between  $mss$  shape derived from optical measurements and Ka-band that can be exploited to infer an effective fourth-order (mean squared curvature)  $msc$  correction. At 10 m/s, a numerical evaluation leads to  $msc \simeq 1200$ , to be compared with stereo-photograph estimates of sea surface curvature (figure 11 in [22]) or other mathematical approaches (figure 5.12 in [23]).

An additional observation is the stronger dependence of this  $\Delta mss_{\text{shape}}$  with wind speed where we observe a nearly quadratic dependence in comparison to the more linear dependency of  $mss$  with wind speed. Thus the Ku- and Ka-band difference data already indicate a means to infer the variable production of rougher surface elements at short scale as winds increase. These elements will contribute to enhance the form drag, thus this derived parameter can then become a possible robust proxy to better infer wind stress at the surface and/or the air-sea gas transfer velocity. We also expect that the high-resolution of GPM bi-frequency radar measurements (5 km), coupled with the concurrent SST derived with the on-board GPM passive microwave (GMI) measurements, will allow for the evaluation of surface roughness contrasts across the satellite swath to detect small-scale wave variations that result from air-sea coupling tied to strong meso- and sub-mesoscale SST variations and surface currents (i.e. [24]).

## 4 Conclusion

Global co-localized ocean surface measurements using the Global Precipitation Measurements (GPM) near-nadir dual-frequency Ku- and Ka-band active microwave measurements are analyzed and compared. Focusing on the Ka-band and Ku-band  $\sigma^0$  fall-off properties with incidence angles, these simultaneous measurements are shown to more precisely document differing ocean scattering characteristics for both microwave frequencies. Sensitivity with wind speed and significant wave height is further reported using global comparisons with numerical estimates.

Considering an extended Physical Optics (PO) approach, the interpretation of the differing sensitivity between Ku- and Ka-band near nadir measurements is discussed. As further related to the well known Cox & Munk optical measurements, the combined bi-frequency measurements are shown to possibly efficiently separate long and short scale roughness elements. As presented, this combined high-frequency measurements can further help to infer total sea surface mean squared slope and to more precisely measure the influence of small-scale roughness elements. As reported, differing sensitivity is significantly ob-

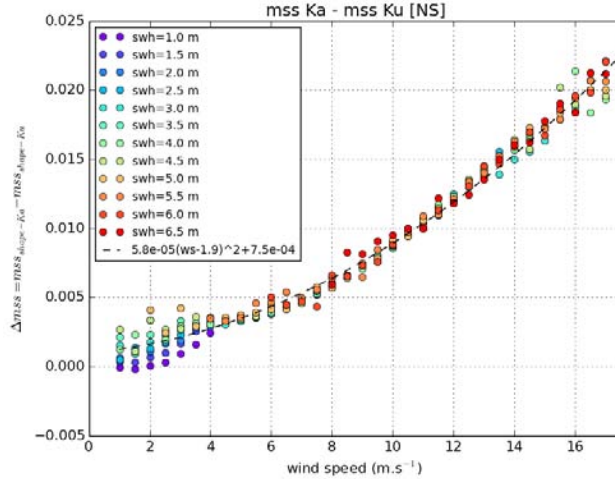


Figure 4: Difference between Ka and Ku mss shape

tained beyond 7 m/s. This is likely explained by the increased occurrence of steep short surface roughness scales, possibly exhibiting high curvature near their crests, but also enhancing the generation surface roughness disturbances generated by breaking waves, including parasitic capillaries.

As foreseen, GPM multi-frequency measurements, including both active and passive microwave observations, may serve essential practical analysis for investigations of various aspects of the air-sea interactions and remote sensing issues.

## References

- [1] B Chapron, K Katsaros, T Elfouhaily, and D Vandemark. A note on relationships between sea surface roughness and altimeter backscatter. *Air-Water Gas Transfer*, pages 869–878, 1995.
- [2] Tanos Elfouhaily, Douglas Vandemark, Jérôme Gourrion, and Bertrand Chapron. Estimation of wind stress using dual-frequency topex data. *Journal of Geophysical Research: Oceans (1978–2012)*, 103(C11):25101–25108, 1998.
- [3] J Gourrion, D Vandemark, S Bailey, and B Chapron. Investigation of c-band altimeter cross section dependence on wind speed and sea state. *Canadian journal of remote sensing*, 28(3):484–489, 2002.
- [4] J Gourrion, D Vandemark, S Bailey, B Chapron, GP Gommenginger, PG Challenor, and MA Srokosz. A two-parameter wind speed algorithm

- for ku-band altimeters. *Journal of atmospheric and oceanic technology*, 19(12):2030–2048, 2002.
- [5] Ge Chen, Bertrand Chapron, Robert Ezraty, and Douglas Vandemark. A dual-frequency approach for retrieving sea surface wind speed from topex altimetry. *Journal of Geophysical Research: Oceans (1978–2012)*, 107(C12):19–1, 2002.
- [6] Michael H Freilich and Barry A Vanhoff. The relationship between winds, surface roughness, and radar backscatter at low incidence angles from trmm precipitation radar measurements. *Journal of Atmospheric and Oceanic Technology*, 20(4):549–562, 2003.
- [7] Ngan Tran, Bertrand Chapron, and D Vandemark. Effect of long waves on ku-band ocean radar backscatter at low incidence angles using trmm and altimeter data. *Geoscience and Remote Sensing Letters, IEEE*, 4(4):542–546, 2007.
- [8] Xiaoqing Chu, Yijun He, and Gengxin Chen. Asymmetry and anisotropy of microwave backscatter at low incidence angles. *Geoscience and Remote Sensing, IEEE Transactions on*, 50(10):4014–4024, 2012.
- [9] Xiaoqing Chu, Yijun He, and V Yu Karaev. Relationships between ku-band radar backscatter and integrated wind and wave parameters at low incidence angles. *Geoscience and Remote Sensing, IEEE Transactions on*, 50(11):4599–4609, 2012.
- [10] Edward J Walsh, Douglas C Vandemark, Carl A Friehe, Sean P Burns, Djamel Khelif, Robert N Swift, and John F Scott. Measuring sea surface mean square slope with a 36-ghz scanning radar altimeter. *Journal of Geophysical Research: Oceans (1978–2012)*, 103(C6):12587–12601, 1998.
- [11] EJ Walsh, CW Wright, ML Banner, DC Vandemark, B Chapron, J Jensen, and S Lee. The southern ocean waves experiment. part iii: Sea surface slope statistics and near-nadir remote sensing. *Journal of physical oceanography*, 38(3):670–685, 2008.
- [12] Douglas Vandemark, B. Chapron, H. Feng, and A Mouche. Sea surface reflectivity variation with ocean temperature at ka-band using near-nadir satellite radar data. *Geoscience and Remote Sensing, IEEE*, 2015.
- [13] Charles Cox and Walter Munk. Measurement of the roughness of the sea surface from photographs of the sun’s glitter. *JOSA*, 44(11):838–850, 1954.
- [14] Pavel A Golubkin, Bertrand Chapron, and Vladimir N Kudryavtsev. Wind waves in the arctic seas: Envisat and altika data analysis. *Marine Geodesy*, 2014.

- [15] FC Jackson, WT Walton, DE Hines, BA Walter, and CY Peng. Sea surface mean square slope from ku-band backscatter data. *Journal of Geophysical Research: Oceans (1978–2012)*, 97(C7):11411–11427, 1992.
- [16] Bertrand Chapron, V Kerbaol, D Vandemark, and T Elfouhaily. Importance of peakedness in sea surface slope measurements and applications. *Journal Of Geophysical Research Oceans*, 105(C7):17195–17202, 2000.
- [17] O. Boisot, F. Nouguier, B. Chapron, and C.-A. Guerin. The go4 model in near-nadir microwave scattering from the sea surface. *Geoscience and Remote Sensing, IEEE Transactions on*, 53(11):5889–5900, Nov 2015.
- [18] Ngan Tran and Bertrand Chapron. Combined wind vector and sea state impact on ocean nadir-viewing ku-and c-band radar cross-sections. *Sensors*, 6(3):193–207, 2006.
- [19] V Kudryavtsev, Bertrand Chapron, and V Makin. Impact of wind waves on the air-sea fluxes: A coupled model. *Journal of Geophysical Research: Oceans*, 119(2):1217–1236, 2014.
- [20] Bertrand Chapron, D Vandemark, and T Elfouhaily. On the skewness of the sea slope probability distribution. *Gas Transfer at Water Surfaces*, pages 59–63, 2002.
- [21] Michael S. Longuet-Higgins and R. P. Cleaver. Crest instabilities of gravity waves. part 1. the almost-highest wave. *Journal of Fluid Mechanics*, 258:115–129, 1 1994.
- [22] MV Yurovskaya, VA Dulov, Bertrand Chapron, and VN Kudryavtsev. Directional short wind wave spectra derived from the sea surface photography. *Journal of Geophysical Research: Oceans*, 118(9):4380–4394, 2013.
- [23] Sébastien Guimbard. *Interprétation et modélisation de mesures a distance de la surface marine dans le domaine micro-onde*. PhD thesis, University of Versailles-Saint-Quentin-en-Yvelines, 2010.
- [24] Nicolas Rasclé, Bertrand Chapron, Aurélien Ponte, Fabrice Ardhuin, and Patrice Klein. Surface roughness imaging of currents shows divergence and strain in the wind direction. *Journal Of Physical Oceanography*, 44(8):2153–2163, 2014.